communications engineering

A Nature Portfolio journal

Article

Article in Press

https://doi.org/10.1038/s44172-026-00792-4

Non-invasive cardiac sensing via an acoustic Helmholtz resonator cavity with electrocardiogram waveform reconstruction

Check for updates

Paul D. Schmalenberg[1] ✉, Hossein Hamidi Shishavan[1], Parveen Singh[1], Kleanthis Avramidis[2], Frederico M. Q. Severgnini[1], Bryan Pardo[3], Taehwa Lee[1] & Ercan M. Dede[1]

Physiological markers are a primary source of prognostic health monitoring systems. Specifically, with heartbeat sensing, many ailments may be identified in their nascent stage. In clinical settings, the human heartbeat is measured by way of an electrocardiogram (ECG). Common metrics for heartbeat analysis include the heart rate (HR), or average beat-to-beat value over time, and heart rate variability (HRV), or variation of beat-to-beat intervals over time. In day-to-day cardiac monitoring, contact-based sensing techniques are realized using various wearable technologies. Here, we present the design, experimental testing, and proof-of-concept validation of a passive acoustic Helmholtz resonator cavity for heartbeat sensing in the [50-120] Hz frequency range and determination of inter-beat interval (IBI) in a non-invasive manner using sound. Integral to this sensing process, a unique neural network-based machine learning algorithm is exploited to reconstruct the ECG waveform from the resonator-enhanced acoustic signal. The system achieved a HR estimation error of 4.23 ± 4.50 BPM and an R-peak timing mean absolute error (MAE) of 6.50 ± 53.17 ms relative to a simultaneously acquired reference ECG. The potential extension of the engineered sensor hardware plus software system for future non-invasive cardiac biomonitoring of seated users in a dynamic vehicle environment is discussed.

Heart-related health issues, ranging from atrial fibrillation to cardiac arrest, are serious and increasingly prevalent. With aging populations[1], the importance of regular and accurate health monitoring methods for the prognosis of such ailments in real-world settings is growing. Importantly, heart-related medical conditions have been identified as a possible leading factor in vehicle crashes[2]. Proactive health monitoring systems inside of a vehicle have been explored in various research scenarios[3–6], establishing that heart monitoring could help prevent automotive related near-miss events and accidents due to heart conditions. Various relevant heart-related biomarkers are identified in the literature based on electrocardiogram (ECG) characteristics, heart rate (HR), heart sound, and ejection fraction[7–11]. Studies have shown a high correlation between the interval between two successive peaks in heart beats and an impending cardiovascular ailment like sudden cardiac arrest[12]. A significant amount of research on this relationship also indicates that the measurement of the cardiac inter-beat interval (IBI) and subsequent heart rate variability (HRV) determination is a predictor of different heart-related conditions and disease[13–16]. The accurate determination of bio-signals like HR, IBI, and HRV is therefore important and lays the foundation for accurate health prognosis.

In clinical practice, HRV is commonly calculated indirectly by measuring the electrical activity of the heart using an ECG. One cycle of depolarization and repolarization in an ECG is called the PQRST sequence, as shown on the left hand side of Fig. 1. The PQRST sequence comprises various waves and complexes including the P-wave, which reflects atrial depolarization. The QRS complex then reflects ventricular depolarization, and the T wave reflects ventricular repolarization[17]. Years of investigation in the medical field have resulted in this understanding of the PQRST sequence. A HRV value may further be estimated by measuring the IBI, which is the temporal separation of two successive R-peaks in the QRS-

[1]Electronics Research Department, Toyota Research Institute of North America, Ann Arbor, MI, USA. [2]Department of Computer Science, University of Southern California, Los Angeles, CA, USA. [3]Department of Computer Science, Northwestern University, Evanston, IL, USA. ✉e-mail: paul.schmalenberg@toyota.com

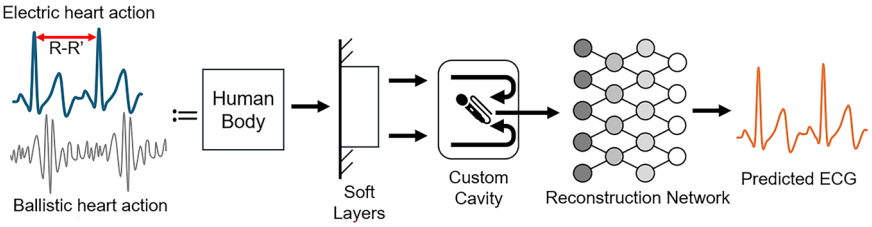


Fig. 1 | Overall cardiac sensing framework. Heartbeats generate an ECG signal (with PQRST sequence) and associated pressure wave from ballistic action (left image). The pressure wave travels from the body, through soft layers of clothing and seat fabric, into the custom Helmholtz resonator which enhances heart-associated sounds, and is converted to a digital pressure wave recording via a transducer. The recording is fed into a neural network (second image from right) that outputs a reconstructed ECG signal (right image), which is compared with a ground truth ECG that is measured using standard medical electrodes.

complex. Thus, for precise determination of HRV, accurate measurement of IBI is imperative.

An ECG test is the "gold standard" for measuring HR activity. The interval (or IBI) between two adjacent R-peaks of a QRS-complex, as shown on the left hand side of Fig. 1, will logically vary over time giving rise to HRV. The HRV accuracy depends on the correctness of the shape of the individual and subsequent QRS-complex waveforms. Clinically, to acquire stable and clean ECG signals, a subject is recommended to be laying stationary and wearing dedicated electrodes with gel placed directly on the torso. Thus, the conventional method of ECG sensing poses a challenge for continuous measurement of HRV in a non-invasive manner. Various research groups have tried to devise different methods of HRV sensing using various techniques like ballistocardiography[18], ultrasound[19], radar[20,21], human voice analysis[22], direct static imaging[23,24], optical sensing[25], and facial video imaging[26], to name a few. A deeper review of non-invasive techniques for HR sensing follows.

Non-contact radar sensing has been extensively studied for physiological monitoring, particularly for respiration and HR estimation using Doppler and FMCW radars. Li et al.[27] review radar sensor designs, signal models, and challenges related to motion and clutter, while Islam et al.[28] provide a more recent overview emphasizing multi-subject monitoring, interference mitigation, and robustness in real-world environments. In the study by Oh et al.[20], they present a Doppler radar-based setup. Their reported accuracy was high, 97.8% mean sensitivity and 96.2% positive predictivity, but these results were in a controlled chamber with electromagnetic isolation, which are conditions that are not easy to replicate in day-to-day situations let alone dynamic vehicle environments. In other radar-related work for the measurement of HRV[21], researchers demonstrate stand-off measurement distances of two meters, but only for an overall HR measurement. The system also was reported to require frequent calibrations to keep it tuned.

Interestingly, the use of the human voice has also been explored as a means for non-invasive sensing of HRV, where Mesleh et al.[22] used vowel speech production to establish a relationship with heart activity. Potential drawbacks include the level of accuracy in extracting the HR signal and the requirement for the measurement target to be continuously speaking.

Other studies using image-based non-invasive approaches[23,24] involved the capture of still images from charge-coupled device (CCD) and infrared cameras. This image information was then used to obtain arterial pulse information for temporal and frequency analysis and HR peak acquisition. These studies show drawbacks related to motion artifacts which required the use of identification markers to provide a reference for the camera system and limitations of IBI resolution tied to camera frame rate. Hence, HR sensing was performed by collecting and analyzing a buffer of images, and the measurement results were therefore not real-time.

The use of optical sensing to gauge HR activity has been further explored in[25], where the experimental setup comprised a simple subwoofer to play audible and inaudible audio of heartbeat sounds. Despite its promise, the concept has not been proven through actual human testing, and the authors of this study mention utilizing the sensing method in a stethoscope-like device in the future. In[26], Chen et al. provide a comprehensive review of remote photoplethtysmography (i.e., the use of an optically obtained plethysmogram) to estimate HR. Besides the effect of lighting artifacts, they identify a critical issue of handling large amounts of data to store related video since most of the studies have only considered uncompressed videos as the base data format to evaluate HR. Speckle plethysmography has also been used for remote HR monitoring[29], but challenges remain with simultaneously reducing measurement error and maintaining eye safety standards.

In acoustic-based studies using a near-ultrasound transmitter-receiver system to measure body surface movement from heart action, Wang et al. utilize a digital beamforming array with a linear array of MEMS microphones to remotely detect the heart rate of multiple subjects simultaneously[30]. However, specific R-peak localization accuracy is degraded making the result difficult to use for determination of IBI.

In an interesting study, Dai et al. use a cylindrical cavity structure [31] as a replacement for a stethoscope to capture the heart sound directly. A meta-unit cell concept is utilized to condense the size of a sub-wavelength resonant structure. Here, Dai et al. show that the acoustic heart sound may easily couple through clothing such that a contact-based but non-invasive method can be leveraged for HRV sensing. Related to in-vehicle applications, Chiang et al. propose a distributed acoustic sensor system augmented by a deep learning network to determine seat occupancy[32], although specific biomarkers like heart rate are not calculated.

To summarize, electrodes (or wearable patches with electrode gel) are extensively used in medical settings for acquiring high-quality HR/HRV data[33]. Non-invasive sensing approaches are thus alternatives to the gold standard contact-based acquisition technique. However, the various aforementioned challenges identified in the prior literature appear to limit the ease of use, accuracy, or computational efficiency of non-invasive sensing methods. Therefore, the contribution of this study includes the design, experimental testing, and proof-of-concept validation of an acoustic Helmholtz resonator for cardiac sensing in a non-invasive manner by localizing individual R-peaks in time using sound. Integral to this sensing process, a unique neural network-based machine learning algorithm is exploited to generate a synthetic ECG waveform that is built from the resonator-enhanced acoustic signal. The synthetic ECG waveform then allows for straightforward extraction of the key cardiac HR, IBI, and HRV metrics.

Results

In this section, we explain how our sound-based sensor plus machine learning technique provides for continuous measurement of beat-to-beat heart rate intervals in ambient conditions, non-invasively, and with high accuracy. In the cardiac sensing framework (see Fig. 1), we employ an acoustic Helmholtz resonator that is integrated into the vehicle seat and coupled closely to the occupant. The benefit of the acoustic Helmholtz resonator approach is that the resonance of the cavity can be tuned to align with the HR frequency range of interest. The resulting acoustic sound is then recorded via a cavity-embedded piezo-acoustic sensor, and the output

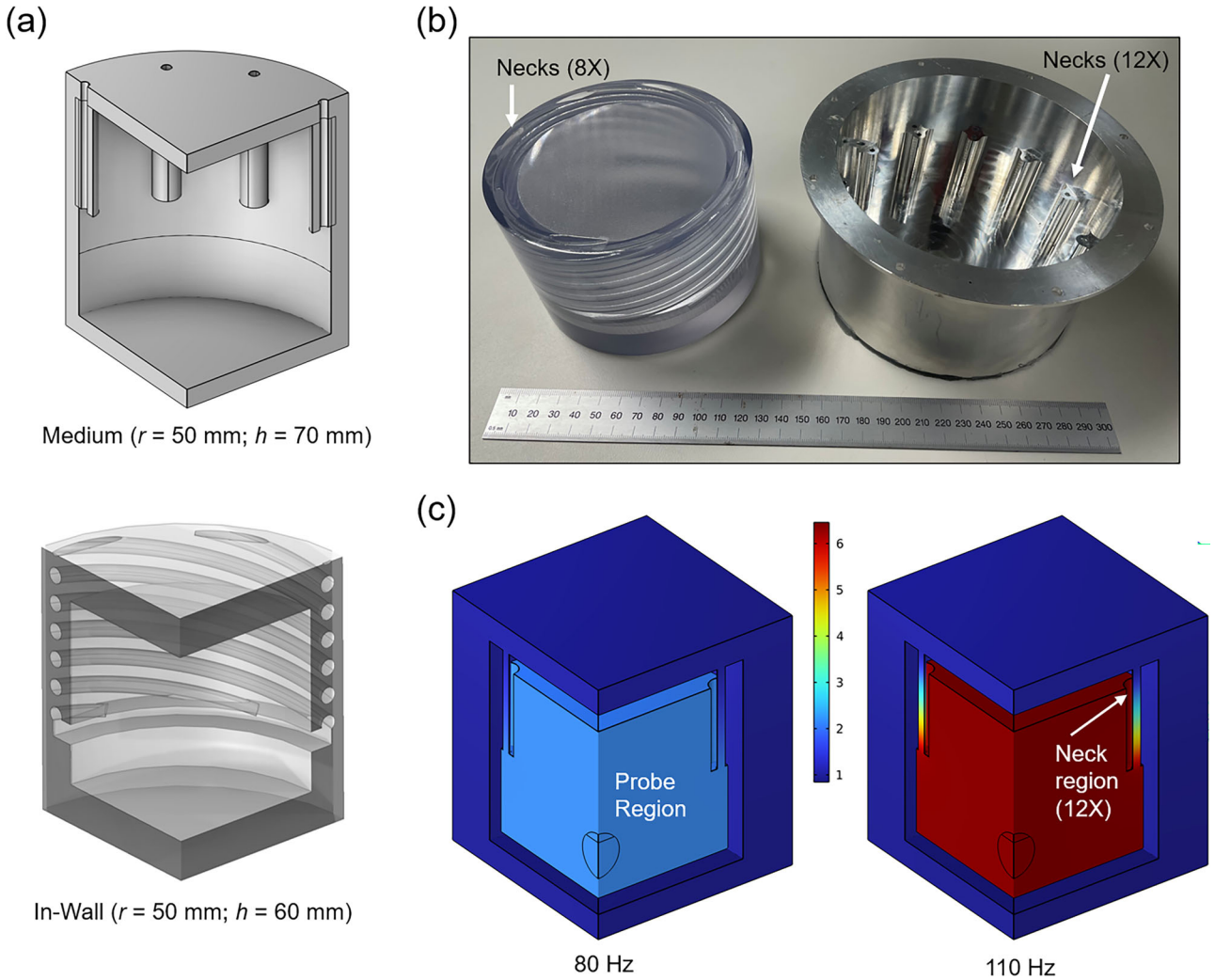


Fig. 2 | Acoustic Helmholtz resonators considered in this study. a One-quarter models of designed resonator geometries with internal air domain dimensions including radius, *r*, and height, *h*. The upper model is one-quarter symmetric, while the lower model is cut away to visualize internal details. **b** Perspective views of in-wall additively manufactured polymer resonator with helical necks (on left) and large size fabricated Al resonator shown prior to closure and seat mounting to reveal internal neck region details (on right). **c** Representative absolute total acoustic pressure numerical results (units: Pa) for small size resonator cavity at off-resonance (80 Hz) and on-resonance (110 Hz) frequencies.

digital recording is fed to an ECG waveform reconstruction algorithm. For the subsequent analysis of the acquired acoustic signal, we adapted a neural-network-based approach derived from the one-dimensional (1-D) convolutional time-domain audio separation network (ConvTASNet)[34,35] to estimate the HR and HRV values. This algorithm relies on QRS-complex peak detection since this peak is the most reliably extracted feature to estimate HR/HRV. The detection of the QRS-complex peak from an acquired signal has been studied by various groups with signal processing algorithms based on nonlinear transforms[36], Fourier and wavelet transforms[37], and machine learning techniques plus neural networks[38–42]. Accordingly, we evaluated reconstruction performance using beat-level timing accuracy and heart-rate estimation error when compared with a ground truth ECG signal acquired using standard medical electrodes.

Acoustic Helmholtz resonator cavity response

To avoid invasive measurement techniques in a vehicle environment, we propose a proximity device integrated within a car seat that is very near to the measurement target, but not physically touching the human body; see the soft layers and custom cavity images in Fig. 1. Instead of a single layer of clothing such as a shirt or sweater[31], several layers of material, including clothing plus additional layers of seat material, are positioned between the body and the acoustic sound measuring device. The Helmholtz resonator then provides HR filtering via resonant frequency enhancement and off-resonance damping.

Figure 2 shows two representative acoustic Helmholtz resonator designs, fabricated prototypes, and numerical modeling results. The details of a spring-mass system analysis for each resonator design, the fabrication method, and the numerical modeling approach are provided in the Methods section. Two Helmholtz resonator designs are explored. First, a resonator that is easily computer numerical control (CNC) machined out of metal is investigated. Second, a more complex resonator with necks that are integrated into the cavity wall and fabricated from a photo-polymer via additive manufacturing is explored for further size and weight reduction. Three sizes of the metal resonator (i.e., small, medium, and large) are considered. A single configuration of the photo-polymer resonator (i.e., in-wall) design is fabricated. Each metal resonator has 12 thin straight necks equally spaced around the periphery of the cavity. The in-wall resonator has eight necks embedded in the cavity wall with each neck coiling 0.8 turns around the circumference of the cavity over 288°. Design parameters for each resonator are provided in Table 1. Note that the in-wall resonator has a 61.7% internal volume reduction and 49.6% weight reduction relative to the large size cavity.

Table 1 | Helmholtz resonator physical parameters plus resonant frequency

	Small Resonator	Medium Resonator	Large Resonator	In-Wall Resonator
Cavity Radius	50 mm	50 mm	70 mm	50 mm
Cavity Height	60 mm	70 mm	80 mm	60 mm
Neck Radius	1.5 mm	1.5 mm	1.5 mm	2.5 mm
Neck Length	36 mm	41 mm	46 mm	280 mm
Number of Necks	12	12	12	8
End Correction	4.32 mm	4.32 mm	4.32 mm	4.80 mm
Mass	0.72 kg	0.77;kg	1.27 kg	0.64 kg
Resonant Freq., Measured	112 Hz	98 Hz	60 Hz	N/A
Resonant Freq., Circuit	114.4 Hz (2.1%)	99.9 Hz (1.9%)	63.4 Hz (5.7%)	58.6 Hz
Resonant Freq., Numerical	110 Hz (-1.8%)	96 Hz (-2.0%)	58 Hz (-3.3%)	54 Hz

Reported resonant frequency values are experimentally measured, calculated using the mechanical spring-mass circuit analysis, and numerically computed using the finite element model. Note that percentage difference from the measured resonant frequency value is listed in parenthesis next to each circuit analysis and numerical model result, and the in-wall resonator was not experimentally measured.

A simple circuit model derived from a mechanical spring-mass system is used to set basic cavity and neck parameters while targeting a heart sound frequency band of ~ 10–100 Hz. These parameters were further adjusted based on requirements for in-vehicle seat installation and heart-cavity alignment for different subject torso sizes. A thermo-viscous acoustics numerical model assuming linearized Navier-Stokes equations is additionally solved for each resonator design to predict wide-band performance. Models for the metal resonators exploit one-quarter symmetry, Fig. 2a, upper image. The in-wall resonator was modeled in full, and the lower image in Fig. 2a shows a one-quarter view to visualize the resonator internal details. Perspective views of the fabricated in-wall Helmholtz resonator and a large-sized resonator are shown in Fig. 2b; note that the metal resonator is shown prior to final closure of the cavity with a bottom end plate (bolted to the flange) in order to visualize the internal necks of the device. Representative absolute total acoustic pressure results from the numerical model for the small-sized resonator design are shown in Fig. 2c on the left and right at frequencies of 80 Hz and 110 Hz, respectively. Observe that the internal absolute total acoustic pressure levels are ~ 3 × lower at 80 Hz (off-resonance) when compared to 110 Hz (on-resonance). Thus, at resonance there is strong coupling into the device air cavity, as intended. The target resonant frequency for the small, medium, large, and in-wall cavities is 63 Hz, 100 Hz, 114 Hz, and 59 Hz, respectively, based on the analytical design method.

To validate the design of the metal resonator cavities, the low frequency acoustic transfer function for each device was measured; note that the in-wall polymer resonator design was not experimentally tested since fabrication was not completed in time for evaluation. Figure 3 shows the results from the experimental testing compared with both the mechanical spring-mass system analysis and numerical modeling results. An excellent match is achieved between experimental, analytical circuit-model, and numerical results in Fig. 3 with the resonant frequency of the small-sized resonator predicted within 2.1% across all approaches versus 2.0% for the medium-sized resonator, and 5.7% for the large-sized resonator. Any differences between the analytical, numerical, and experimental results in the resonant frequency may be attributed to minor differences in the cavity volume from small adjustments to the geometry for better tooling access during CNC machining. Numerically predicted resonant gain is systematically higher than the experimentally measured results (up to ~ 7.5%, for the smallest resonator), as well, which could be an effect of having a slightly imperfect lid seal, the addition of an access port for the acoustic probe, or additional minor damping in the as-built device.

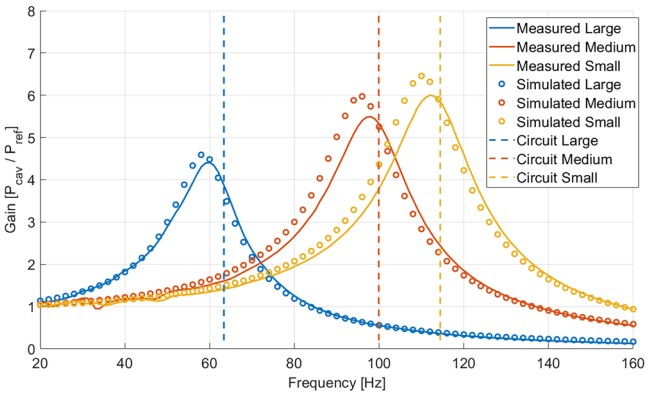


Fig. 3 | Comparison of acoustic transfer functions. Results from experimental measurements (solid lines), thermo-viscous simulations (circle markers), and equivalent spring-mass analyses for the three (small, medium, and large) Al metal resonators from Table 1 (vertical dotted lines) are plotted here.

Acoustic heartbeat acquisition

Data were collected from 13 human volunteers after obtaining informed consent from each participant. All procedures adhered to the guidelines set forth by Toyota Legal One and approved by Toyota Motor North America Office of Privacy. All experimental sessions were conducted in a quiet lab environment. Participants were seated on a vehicle seat in which the acoustic Helmholtz resonator was integrated into the seat back structure; additional description is available in the Supplementary Information. The resonator was installed without modifying the front seat upholstery, thereby preserving realistic coupling conditions. Each session took up to 40 min, and participants were free to pause or terminate the experiment at any time. They were instructed to minimize sudden movements while maintaining normal breathing, with no restrictions on clothing.

The medium-sized resonator was used as a collection device, as the small-sized resonator's frequency band was further from our frequencies of interest. The large resonator's face is too broad to eliminate air gaps between the face plate and the irregular surface of the human body, which significantly reduced the sound coupling efficiency between the body and the resonator. As a benchmark, an ECG signal was simultaneously captured using standard electrodes and recorded for later comparison. Raw acoustic signal data was de-noised with basic signal processing techniques to bring the cardiac action to the forefront. Details of the data acquisition method and processing are available in the Methods section.

Comparison between the raw audio signal and processed audio signal is provided in Fig. 4. The raw audio signal is dominated by very low frequency noise from the environment, which masks the small-signal higher frequencies of interest that become apparent when a high-pass filter is applied. A large amplitude envelope in the processed audio signal following each R-peak in the processed ECG signal, shown in Fig. 4, demonstrates the

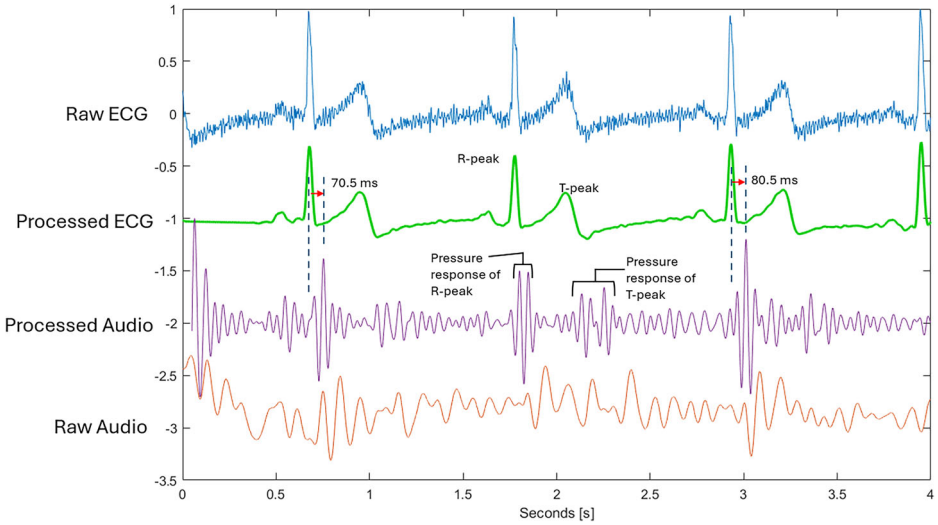


Fig. 4 | Comparison of the raw and processed ECG and audio waveforms. A representative four second window is shown. Each waveform is normalized within its own channel and offset in the y-axis for clarity.

capture of the ballistic heart action from the sensor. This S1 sound has been shown to be associated with ECG R-peaks[43]. The acoustic pressure wave will always follow the R-peak with some delay due to the length of time for the heart to contract and the pressure wave propagation delay. However, note that the peak amplitude of the pressure wave does not correspond directly with the R-peak of the ECG waveform. As an example, the delay between the processed ECG R-peak and the processed audio maximum for the first and third beats in Fig. 4 differ by 70–80 ms. Furthermore, while the processed audio has a raised envelope related to the second processed ECG R-peak, there is no well-defined maximum. Possible reasons for this include superposition of other bodily functions such as gastrointestinal processes, breathing, or blood flow in arteries away from the heart which create noise within the same frequency band and a R-peak width that is much shorter in time than a wavelength at the frequency of interest. Non-invasive acoustic monitoring of bio-signals could be further hindered by environmental noise, such as a vehicle engine or friction-induced sound from movement of the user over the sensor. Due to this, localizing the processed ECG R-peak in time with a high degree of accuracy using a simple threshold for the processed acoustic signal is not possible. Therefore, we investigate a more advanced method using a data-driven approach.

Data-driven ECG waveform reconstruction

The problem of estimating the ECG from the processed audio signal is similar to the audio source separation problem, where one extracts a single audio signal from a recording containing a mixture of signals. Therefore, we based our method on a deep-learning-based approach source separation: Conv-TASNet[35]. Training the Conv-TASNet model is performed following the procedure outlined in the Methods section. Processed audio and ECG waveforms, as shown in Fig. 4, are used as the basis for the training dataset, which is augmented at each epoch by mixing white noise at varying power levels into each waveform snippet. About 215 minutes of data were used in the training process, with 45 minutes held for validation and 168 minutes held for testing; refer to the Methods.

Figure 5 shows an example of the neural network estimation (ECG Prediction), compared to the ground truth (ECG Measurement), as well as the difference between both signals. As detailed in Table 2, this example is from the test portion of the data which was left out of the training and validation sets. Table 3 presents per-participant evaluation, including R-peak timing MAE and HR estimates obtained from the reconstructed ECG compared with the reference processed ECG. Aggregated across all participants, the proposed neural network yielded a heart-rate estimation error of 4.23 ± 4.50 BPM and an R-peak timing MAE of 36.50 ± 53.17 ms.

In addition to beat-level performance, we investigated model interpretability and waveform-level reconstruction fidelity. A 1-D Grad-CAM analysis was computed at the attention layer and projected on to the time axis to yield normalized attribution scores. As shown in the Supplementary Information, the Grad-CAM attribution is localized around beat-related ECG transients, with greater occurrence shortly after the R-peak, consistent with mechano-acoustic consequences of ventricular activation.

Beyond R-peak localization, the reconstructed ECG morphology was evaluated using Pearson correlation and normalized Dynamic Time Warping (DTW) distance metrics; see the Supplementary Information. These results suggest, despite relying solely on acoustically measured signals that capture only the mechanical consequences of cardiac activity, the neural network is able to reconstruct (i.e., predict) the ECG waveform with high fidelity, as reflected by low DTW (0.033) distances and high correlation (0.74) metrics.

Discussion

In this study, we demonstrated a proof-of-concept implementation of a non-invasive method to recover the ECG waveform from an occupant in a vehicle seat via an acoustic Helmholtz resonator-based sensor. The acoustic resonator is designed using a simplified spring-mass analysis and finite element numerical methods for low-frequency (10–100 Hz) operation while minimizing design complexity. A neural network architecture based on a source-separation concept allows for the isolation of the pressure wave generated by cardiac ballistic action and reconstruction of the entire ECG sequence despite several competing acoustic processes within the human body. Data for the training set is collected via a custom resonator to demonstrate a real-world use case where the pressure wave propagates through several layers of material. A close match between the measured ECG waveform and a reconstructed ECG waveform is achieved. This high level of agreement is supported by data that were collected across 13 participants. While the results demonstrate robust performance in a lab setting, degradation in accuracy may be expected in a dynamic vehicular environment due to a qualitative increase in noise from the vehicle engine, road-tire interface, occupant motion-induced artifacts, and external sounds.

We present this approach as a potential alternative to in-vehicle HR detection schemes that utilize radar sensors or cameras. Unlike approaches that depend on detecting very small human motions or subtle skin color variations, the proposed system utilizes acoustic sensing embedded within the seat. This design may offer advantages under certain operating conditions. However, a systematic evaluation of its relative robustness in highly dynamic or chaotic driving environments remains an important direction for future investigation.

The combined sensor hardware and neural-network-based waveform reconstruction framework is designed to be extensible to noisier acoustic environments typical of real driving scenarios. With the sensing hardware

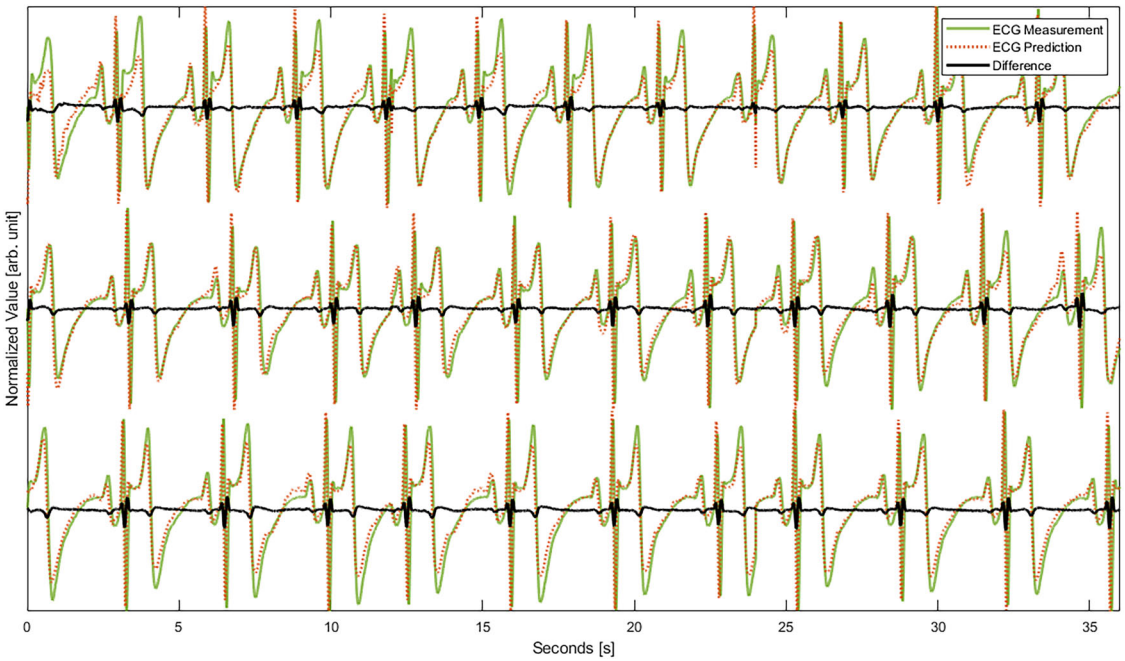


Fig. 5 | Comparative plot of ECG waveforms. A representative 108 s window of neural-network reconstructed ECG waveform (i.e., prediction) generated from the processed audio compared against the processed experimental ECG signal measurement obtained using standard electrodes.

Table 2 | Length of dataset within each training split

Split	Length of Data
Training	215 min and 32 s
Validation	45 min and 18 s
Test	168 min and 06 s

Table 3 | Subject-level evaluation of R-peak timing

ID	MAE (ms)	HR^{pred} (BPM)	HR^{gt} (BPM)
P1	73.27	55.52	56.50
P2	161.04	53.27	54.80
P3	66.32	57.33	58.10
P4	121.86	41.40	51.20
P5	7.84	42.63	57.30
P6	1.21	64.55	64.90
P7	1.71	81.65	88.50
P8	2.23	56.10	60.30
P9	2.66	48.00	50.10
P10	2.69	61.50	62.30
P11	22.84	66.80	74.20
P12	9.16	65.70	67.00
P13	1.64	63.90	64.70
Avg	36.50 ± 53.17	58.33 ± 10.91	62.30 ± 10.29

Each subject's beat to beat MAE, predicted HR, HR^{pred}, based on reconstructed ECG waveform, and the measured ground-truth ECG HR, HR^{gt}.

integrated within the seat, future work can explore the extension of our generative model to tackle this noisier, low signal-to-noise ratio (SNR), environment and better understand the minimum dataset size necessary to maintain reliable performance over varied vehicle speed and road surfaces.

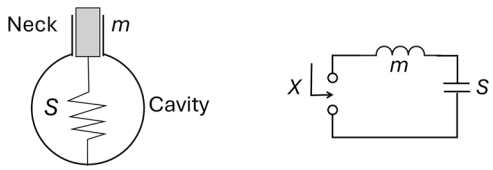


Fig. 6 | Helmholtz cavity resonator circuit model. Two representations of Helmholtz resonators including the mechanical mass and spring system diagram (left) and the equivalent circuit schematic (right).

Method

Acoustic Helmholtz resonator design

The Helmholtz resonator is a cylindrical-shaped cavity device with multiple openings that exhibits air resonance attributed to the motion of fluid trapped inside these neck regions, where this fluid then interacts with the larger fluid volume of the main cavity; refer to Fig. 2b. Traditionally, for acoustics applications, a Helmholtz resonator is primarily used as a noise reduction component in machinery applications and acoustic spaces at micro-to-macro scales[44–47]. Helmholtz resonators have recently also been heavily used for acoustic energy harvesting with a range of investigations exploring variations in geometry, design, and material[48–53]. Here, a Helmholtz resonator is designed such that its resonant frequency is near to the HR target frequency to amplify a particular sound that is distinct from the ambient noise. We specifically couple the Helmholtz resonator with a piezoelectric-based pressure-acoustic sensor to sense this human heartbeat sound. This is challenging assuming the usable frequencies from a singular heartbeat in isolation are below 100 Hz.

Mechanical spring-mass system analysis. For analytical evaluation of the Helmholtz resonator, we assume a standard system as depicted in Fig. 6 (left side image), where a cavity with rigid walls has an internal air volume and a neck opening. The dimensions of the cavity are presumed to be considerably smaller than the signal wavelength of interest. We approximate the resonator as a mechanical-acoustic system that can be represented using a spring-mass-damper arrangement. If we consider an equivalent circuit, Fig. 6 (right side image), then the impedance of the

system is $X = m\omega - S/\omega$, and resonance of the circuit occurs at a frequency, f_o, when $X = 0$ such that,

$$f_o = \frac{1}{2\pi}\sqrt{\frac{S}{m}}, \tag{1}$$

where

$$S = \rho_o c^2 \frac{A_{eff}^2}{V}, \tag{2}$$

$$m = \rho_o A_{eff} L\prime, \tag{3}$$

therefore

$$f_o \propto \frac{A_{eff}}{VL\prime}. \tag{4}$$

In the above set of equations, c is the speed of sound in the fluid within the cavity and necks, ρ_o is the density of the filling material, V is the volume of the fluid inside the cavity, and $A_{eff} = nA$ is the effective cross-sectional area of the neck, where n is the number of same sized necks of cross-section area, A. Additionally, $L\prime$ is the effective length of neck, which is the measured length of the neck plus an end correction, which considers the neck's geometrical shape, neck cross-section, and inside-outside physical interactions of the fluid mass in the neck[54].

A challenge for this resonator design is matching the device resonance to the low frequency content of the heartbeat sound, as explained above. To decrease the resonant frequency of the resonator, we can increase the cavity volume, increase the neck length, or reduce the neck cross sectional area, based on (4). In our application, the final resonator size is limited by practical considerations of eventual installation into a typical vehicle seat.

Various groups have investigated different methods to reduce the resonant frequency of the resonator for given outer dimensions using modifications to the neck of the device[55–59]. The majority of these papers study modifications to neck design including internally extending the neck, tapering the neck profile, or a spiral-shaped neck, to name a few. However, there is a trade-off established in these studies between the volume, V, of the fluid inside the cavity and reductions due to increasing the effective neck length, $L\prime$. By helically coiling the neck within the cavity, the volume of the cavity is reduced by the presence of the neck.

Our easily CNC machined metal resonator designs minimize the occupied cavity volume by placing the neck as close to the cavity wall as possible. Although a multi-neck design increases the effective neck aperture thus increasing the resonant frequency, we distribute multiple necks around the periphery of the device to create a larger interface surface for acoustic signal acquisition. Neck area is then minimized by setting the neck radius to the minimum allowed by the fabrication process. For our photo-polymer additively fabricated resonator design, we envision embedding the neck within the cavity wall. Since the neck is now completely removed from the cavity interior, we can increase the length, $L\prime$, through coiling without reducing the cavity volume, thus achieving a lower resonant frequency without size penalty.

Thus, four resonator designs are considered for fabrication. Dimensions for each resonator are given in Table 1, and these sizes were selected as a trade-off between compactness versus coverage of the frequency range of interest, ~ 10–100 Hz, for the acquired heartbeat sound.

Numerical modeling approach. When the size of the device is much smaller than that of the signal wavelength in a given medium, the above analytical design method may be insufficient to accurately predict device resonance characteristics. Viscous shear waves may need to be considered to achieve accurate modeling. Thus, we numerically model our resonators using a frequency domain finite element analysis in COMSOL assuming thermo-viscous-acoustics physics to capture the effects. We utilize the simulations to confirm the cavity design volume, neck length, and neck cross-sectional area parameters of the resonator, Table 1, produce the expected resonant response relative to analytical predictions. Attention is then paid to the mesh for validation simulations to adequately understand losses associated with viscous and thermal boundary layers.

Resonator fabrication. Solid model geometry for each resonator model is exported from COMSOL and imported into SolidWorks so that the design can be finalized for fabrication. The computer-aided design (CAD) geometry of the model is modified to include a flange on the resonator face without neck holes to create a lid for the metal-based designs; see Fig. 2b. The cavity and lid are CNC machined out of 6061-T6 aluminum (Al). Internal corners of the cavity have fillets applied in the CAD geometry to account for CNC tool size, which slightly reduces the air volume (<2.5%) within the cavity. A slot is machined into the interior of the lid to allow connections to be made to the interior probe. The lid is finally attached to the cavity with eight M3 bolts and nuts to complete the assembly. For the photo-polymer in-wall resonator design, the entire structure is additively manufactured as one piece via stereolithography printing using Somos WaterClear Ultra 10122 material. The exterior is polished so that the internal neck structure is visable.

Resonator characterization. Measurement of the low frequency acoustic transfer function for each metal resonator was completed at a Hottinger Bruel & Kjaer facility. Each resonator was prepared by inserting an acoustic probe, which was sheathed over a microphone (B&K 4187), into one of the slots in the cavity lid. Each resonator was then mounted onto a foam stack to align it with the sound source and reference microphone (B&K 4187). Each microphone is calibrated with a B&K 4231 microphone calibrator.

A low frequency sound source powered by an audio amplifier (B&K 2716) is placed within a tube system. The tube system ensures a flat phase front near the tube opening. The tube is then suspended from hangers by bungee cords for acoustic isolation. A reference microphone is then placed 150 mm from the tube opening, and the resonator is situated on a foam stack a further 150 mm from the reference microphone. The entire setup is placed within a low-frequency acoustic anechoic chamber, as shown in Fig. 7 and the Supplemental Information, Fig. S7. Data is acquired through a B&K 3160 LAN-Xi DAQ using BK Connect acquisition software, which allows for a wide-band noise source for calibration.

ECG waveform reconstruction with neural networks

Non-invasive monitoring and extraction of heartbeat-related information offers several benefits mentioned above, such as improved comfort and convenience for the user. Hence, in this section we propose to recover such information from the recorded audio signal through machine learning. Specifically, we build a model to reconstruct (i.e., predict) the ECG signal

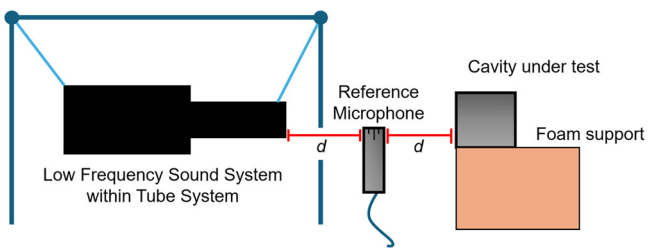


Fig. 7 | Experimental setup for resonator cavity acoustic characterization. Distance d is 150 mm. The reader is also referred to the experimental setup shown in the Supplemental Information, Fig. S7.

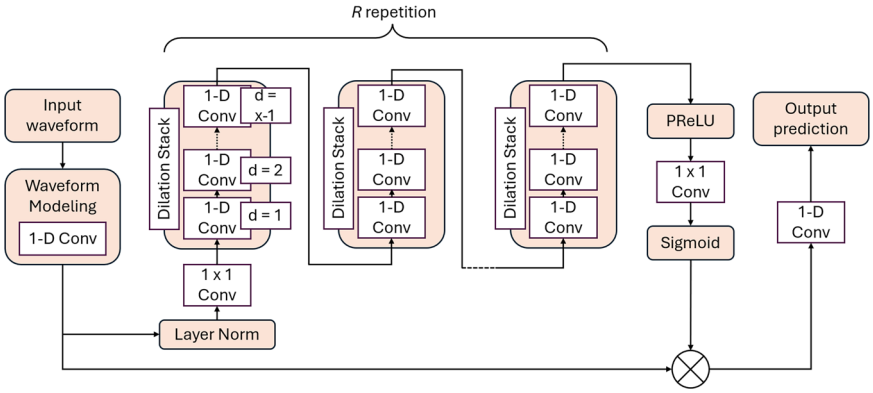


Fig. 8 | Neural network for ECG reconstruction. Schematic of the Conv-TASnet model used to generate the ECG prediction.

from the audio response of the resonator and use the ECG estimation to determine heartbeat information.

Machine learning algorithm. The proposed algorithm takes advantage of the weak alignment between cardiac sounds recorded via the in-cavity sensor and the ground-truth electrocardiogram in order to reconstruct a proxy ECG output, from which heartbeat can be reliably extracted. The framework consists of (a) weak alignment: training and validation of a neural network for ECG reconstruction from input audio recordings, and (b) HR/HRI information extraction from the estimated ECG. We refer to (a) as "alignment", because it regularizes the learning process of extracting heart rate information (as opposed to directly predicting the timestamp of R-peaks) and as "weak" because the ECG can only be partially inferred from cardiac sounds. This weak alignment further reflects the inherent and beat-to-beat-varying temporal delay between electrical depolarization and the ensuing mechano-acoustic response, which would need to be explicitly parameterized in future work. Although biological and environmental factors prevent an exact waveform reconstruction, key elements of interest such as the R-peaks in the ECG are well-correlated with specific documented cardiac sounds. As a result, even without explicit delay parameterization, the weak-alignment formulation preserves sufficient temporal accuracy. As shown in Supplementary Table S1, the resulting timing differences are 36.50 ± 53.17 ms and < 4 BPM, which satisfies ANSI/AAMI EC13 requirements of absolute error < 5 BPM or relative error $< 10\%$ [60].

The architecture of the model shown in Fig. 8 was configured to build upon successful time-domain neural architectures originally developed for audio source separation and reconstruction. This domain was identified due to the acoustic nature of the input and the denoising-oriented reconstruction objective. Specifically, we chose the ConvTASNet model[35], a convolutional network designed for end-to-end source separation, leveraging a fully-convolutional layer architecture. ConvTASNet operates directly in the time domain, avoiding the need for spectrogram-based pre-processing of audio. The architecture begins with an encoder that transforms input signals into a high-dimensional feature space using learnable filters. A temporal convolutional network (TCN) processes these features, capturing long-term dependencies with a stack of dilated convolutional layers. The heart sound waveform has periodic properties in the time domain, so the utilization of kernel dilation is expected to enable the network to more easily capture relevant periodic features observed in the input signal. The TCN outputs are then mapped back to the time domain using a decoder to reconstruct the separated sources. In adapting ConvTASNet for ECG reconstruction, its encoder-decoder structure and temporal modeling are repurposed to extract physiological signal patterns from audio features, having a single output channel of the same dimensionality as the audio input.

Given the trained machine learning model and a pre-processed input audio signal, the proposed framework finally estimates HR/HRV information by calculating R-peak locations, IBI intervals, and HR from the extracted proxy ECG estimation (Fig. 5). The FastNVG algorithm by Emrich et al.[61] is used to estimate the location of R-peaks in the generated output, which works by transforming the ECG into a graph representation[62].

Data collection and pre-processing. In this section, we describe the data collection environment for the pressure-acoustic signal and electrocardiogram. To collect the pressure-acoustic (PA) signal, a PCB Piezotronics 352C68 shear sensing transducer is bonded to the inside of the medium-sized cavity with adhesive tack. A 2 mm layer of Ecoflex 00-20 silicone rubber is cured on the neck interface to assist with coupling of sounds between the resonator and human body. The resonator was then integrated into the seat-back and acoustically coupled to the participant through the vehicle seat, without direct contact with the body. Participants wore typical everyday clothing. The seat upholstery and compliant silicone interface constituted multiple intervening layers between the body and the resonator with a total thickness of 8.5 mm, not including clothing. The transducer is connected to a PCB Piezotronics 482C15 signal conditioner to power the transducer and receive the output, which is then connected to a Biopac DA100C module to record the signal. In parallel to the PA recordings, ECG data is recorded via a three-electrode system, with electrodes placed on the participant's wrists and ankles following the Lead II configuration. The ECG electrodes are connected to the Biopac ECG100C module. Both this module and the DA100C module reside within a Biopac MP160 chassis to allow synchronization of time-stamped samples. Further details of the experimental setup, including pictures, are provided in the Supplementary Information.

Synchronous PA and ECG signals were acquired at a sample rate of 4 kHz, downsampled to 2 kHz, and segmented into four seconds snippets. The PA snippets were first filtered using a 5 Hz steep roll-on high pass filter, then filtered with a Butterworth bandpass filter of order 2 via NeuroKit[63] between 25 Hz and 50 Hz, and then normalized. A 30 Hz low-pass filter was applied to the ECG signal to suppress mains interference, after which the signal was normalized. An example of the frequency content of the signal after this step is shown in Fig. 9.

Data were collected from 13 participants after obtaining informed consent from each participant. All procedures adhered to the guidelines set forth by Toyota Legal One and approved by Toyota Motor North America Office of Privacy. All recordings were conducted in a quiet room, with participants wearing one or two layers of clothing typical of fall attire. Data segments with erroneous amounts of noise due to excessive body movement or readjustment of sensor positioning were excluded from the dataset. As a result, the aggregated remaining data totaled 7 hours and 8 minutes.

Training the neural network. We trained a time-domain model to map the PA waveform to the corresponding ECG waveform using a Conv-TasNet–based architecture. Data were segmented into 4 s windows (50% overlap for train/validation; no overlap for test), and the train/validation/

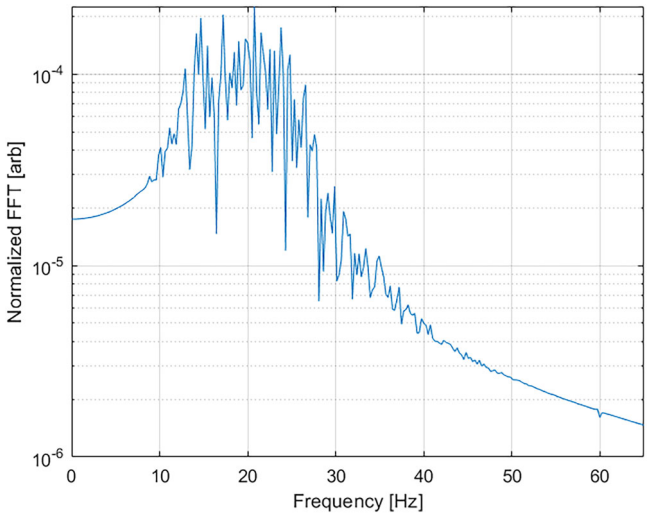


Fig. 9 | Frequency domain representation of Fig. 4. Fourier transform of the four second long 'Processed Audio' time signal in Fig. 4, representing the frequency content after the filtering pre-processing steps.

test split followed Table 2. Data augmentation was performed during training and we applied augmentation by adding white Gaussian noise with SNR randomly selected from {0,30,60,90} dB. The optimization process employed PyTorch with AdamW (learning rate 0.001, weight decay 0.01; batch size 8) and a log-cosh waveform loss (auraloss[64]); the learning rate was reduced by 10 × after five consecutive validation epochs without improvement, and models were trained for 50 epochs. At inference, segment-level outputs were stitched into a continuous reconstructed ECG and post-processed with NeuroKit2's ecg_clean() function at 2 kHz prior to downstream analysis. Full implementation details (architecture specification, software versions, and compute environment) are provided in the Supplementary Information, Sections 1–1.4.

Identifiable Images

Written consent has been obtained from all subjects appearing in images containing identifiable persons, especially figure S5 in the supplementary text.

Ethics

This work involved human subjects in its research. Experiments were approved in advance following our established institutional procedures. This process included consultation with Toyota Legal One, Toyota Motor North America's internal legal team, to ensure compliance with all legal and ethical standards. Additionally, approval was obtained from Toyota Motor North America's Privacy & Governance function to guarantee adherence to privacy regulations in the processing of personal information. Informed consent was obtained from all participants verbally and in writing before any experiments or data collection began.

Data availability

All data collected for training the neural network and all source data used within figures is available at figshare[65] under MIT license.

Code availability

All code for the neural network, network check point, COMSOL models, and code to generate most figures is available on GitHub[66] under MIT license.

Received: 30 January 2025; Accepted: 11 September 2026;
Published online: 06 October 2026

References

1. United Nations, Department of Economic and Social Affairs, Population Division. World population prospects 2022, online edition (2022).
2. Dischinger, P. C., Ho, S. M. & Kufera, J. A. Medical conditions and car crashes. In *Annual Proceedings/Association for the Advancement of Automotive Medicine*, vol. **44**, 335 (2000).
3. Shin, H.-S., Jung, S.-J., Kim, J.-J. & Chung, W.-Y. Real time car driver's condition monitoring system. In *SENSORS, 2010 IEEE*, 951–954 (2010).
4. Mei, Z., Gu, X., Chen, H. & Chen, W. Automatic atrial fibrillation detection based on heart rate variability and spectral features. *IEEE Access* **6**, 53566–53575 (2018).
5. Schires, E., Georgiou, P. & Lande, T. S. Vital sign monitoring through the back using an UWB impulse radar with body coupled antennas. *IEEE Transactions on Biomedical Circuits and Systems* **12**, 292–302 (2018).
6. Zhang, Q. et al. Webcam-based, non-contact, real-time measurement for the physiological parameters of drivers. *Measurement* **100**, 311–321 (2017).
7. Perret-Guillaume, C., Joly, L. & Benetos, A. Heart rate as a risk factor for cardiovascular disease. *Progress in cardiovascular diseases* **52**, 6–10 (2009).
8. Roy, J. K., Roy, T. S. & Mukhopadhyay, S. C.*Heart Sound: Detection and Analytical Approach Towards Diseases*, 103–145 (Springer International Publishing, Cham, 2019).
9. Hasan, R., Ahmed, S. & Afridi, A. Heart sound analysis for detection of cardiovascular diseases (CVDs) through segmentation. *International Journal of Scientific & Engineering Research* **11**, 1–6 (2020).
10. Hammad, M., Maher, A., Wang, K., Jiang, F. & Amrani, M. Detection of abnormal heart conditions based on characteristics of ECG signals. *Measurement* **125**, 634–644 (2018).
11. Dunlay, S. M., Roger, V. L., Weston, S. A., Jiang, R. & Redfield, M. M. Longitudinal changes in ejection fraction in heart failure patients with preserved and reduced ejection fraction. *Circulation: Heart Failure* **5**, 720–726 (2012).
12. Sessa, F. et al. Heart rate variability as predictive factor for sudden cardiac death. *Aging***10**, 166–177 https://doi.org/10.18632/aging.101386.
13. Watanabe, E., Kiyono, K., Yamamoto, Y. & Hayano, J.*Heart Rate Variability and Cardiac Diseases*, 163–178 (Springer Japan, Tokyo, 2017).
14. Haensel, A., Mills, P. J., Nelesen, R. A., Ziegler, M. G. & Dimsdale, J. E. The relationship between heart rate variability and inflammatory markers in cardiovascular diseases. *Psychoneuroendocrinology* **33**, 1305–1312 (2008).
15. Nolan, J. et al. Prospective study of heart rate variability and mortality in chronic heart failure: results of the united kingdom heart failure evaluation and assessment of risk trial (UK-heart). *Circulation* **98**, 1510–1516 (1998).
16. Bouvy, M. L., Heerdink, E. R., Leufkens, H. G. M. & Hoes, A. W. Predicting mortality in patients with heart failure: a pragmatic approach. *Heart* **89**, 605–609 https://doi.org/10.1136/heart.89.6.605 (2003).
17. Hurst, J. W. Naming of the waves in the ECG, with a brief account of their genesis. *Circulation* **98**, 1937–1942 (1998).
18. Mack, D. C., Patrie, J. T., Suratt, P. M., Felder, R. A. & Alwan, M. Development and preliminary validation of heart rate and breathing rate detection using a passive, ballistocardiography-based sleep monitoring system. *IEEE Transactions on Information Technology in Biomedicine* **13**, 111–120 https://doi.org/10.1109/TITB.2008.2007194 (2009).
19. Ambrosanio, M., Franceschini, S., Grassini, G. & Baselice, F. A multi-channel ultrasound system for non-contact heart rate monitoring. *IEEE Sensors Journal* **20**, 2064–2074 (2019).

20. Oh, S. H., Lee, S., Kim, S. M. & Jeong, J. H. Development of a heart rate detection algorithm using a non-contact doppler radar via signal elimination. *Biomedical Signal Processing and Control* **64**, 102314 https://doi.org/10.1016/j.bspc.2020.102314 (2021).
21. Al-Masri, E. & Momin, M. Detecting heart rate variability using millimeter-wave radar technology. In *2018 IEEE International Conference on Big Data (Big Data)*, 5282–5284 (IEEE, 2018).
22. Mesleh, A., Skopin, D., Baglikov, S. & Quteishat, A. Heart rate extraction from vowel speech signals. *Journal of Computer Science and Technology* **27**, 1243–1251 (2012).
23. Chekmenev, S. Y., Farag, A. A., Miller, W. M., Essock, E. A. & Bhatnagar, A. Multiresolution approach for noncontact measurements of arterial pulse using thermal imaging. *Augmented Vision Perception in Infrared: Algorithms and Applied Systems* 87–112 (2009).
24. Takano, C. & Ohta, Y. Heart rate measurement based on a time-lapse image. *Medical Engineering & Physics* **29**, 853–857 (2007).
25. Gurkan, D., Starodubov, D. & Yuan, X. Monitoring of the heartbeat sounds using an optical fiber Bragg grating sensor. In *SENSORS, 2005 IEEE*, 4 (IEEE, 2005).
26. Chen, X. et al. Video-based heart rate measurement: Recent advances and future prospects. *IEEE Transactions on Instrumentation and Measurement* **68**, 3600–3615 (2018).
27. Li, C., Lubecke, V. M., Boric-Lubecke, O. & Lin, J. A review on recent advances in doppler radar sensors for noncontact healthcare monitoring. *IEEE Transactions on microwave theory and techniques* **61**, 2046–2060 (2013).
28. Islam, S. M., Boric-Lubecke, O., Lubecke, V. M., Moadi, A.-K. & Fathy, A. E. Contactless radar-based sensors: Recent advances in vital-signs monitoring of multiple subjects. *IEEE Microwave Magazine* **23**, 47–60 (2022).
29. Herranz Olazabal, J., Wieringa, F., Hermeling, E. & Van Hoof, C. Comparing remote speckle plethysmography and finger-clip photoplethysmography with non-invasive finger arterial pressure pulse waves, regarding morphology and arrival time. *Bioengineering* **10**, 101 (2023).
30. Wang, L. et al. Acoustic sensing for multi-user heartbeat monitoring using dualforming. *IEEE Transactions on Mobile Computing* (2025).
31. Dai, R. et al. Acoustic meta-stethoscope for cardiac auscultation. *APL Materials* **12**, 031109 https://doi.org/10.1063/5.0189552 (2024).
32. Chiang, C.-Y., Zhong, R., Jaber, M. & Hayward, P. A distributed acoustic sensor system for intelligent transportation using deep learning. *IEEE Internet of Things Magazine* **7**, 88–96 (2024).
33. Garvey, J. L. ECG techniques and technologies. *Emergency Medicine Clinics* **24**, 209–225 (2006).
34. Luo, Y. & Mesgarani, N. Tasnet: time-domain audio separation network for real-time, single-channel speech separation. In *2018 IEEE International Conference on Acoustics, Speech and Signal Processing (ICASSP)*, 696–700 (IEEE, 2018).
35. Luo, Y. & Mesgarani, N. Conv-tasnet: Surpassing ideal time–frequency magnitude masking for speech separation. *IEEE/ACM transactions on audio, speech, and language processing* **27**, 1256–1266 (2019).
36. Germán-Salló, Z. & Germán-Salló, M. Non-linear methods in HRV analysis. *Procedia technology* **22**, 645–651 (2016).
37. Ali, M. N., El-Dahshan, E.-S. A. & Yahia, A. H. Denoising of heart sound signals using discrete wavelet transform. *Circuits, Systems, and Signal Processing* **36**, 4482–4497 (2017).
38. Yaseen, Son, G.-Y. & Kwon, S. Classification of heart sound signal using multiple features. *Applied Sciences***8**, 2344 (2018).
39. Chen, W. et al. Deep learning methods for heart sounds classification: A systematic review. *Entropy* **23**, 667 (2021).
40. Toda, D., Anzai, R., Ichige, K., Saito, R. & Ueki, D. ECG signal reconstruction using FMCW radar and convolutional neural network. In *2021 20th International Symposium on Communications and Information Technologies (ISCIT)*, 176–181 (IEEE, 2021).
41. Yamamoto, K., Hiromatsu, R. & Ohtsuki, T. ECG signal reconstruction via Doppler sensor by hybrid deep learning model with CNN and LSTM. *IEEE Access* **8**, 130551–130560 (2020).
42. Arvin, F. & Doraismay, S. Real-time segmentation of heart sound pattern with amplitude reconstruction. In *2010 IEEE EMBS Conference on Biomedical Engineering and Sciences (IECBES)*, 130–133 (IEEE, 2010).
43. Xiefeng, C., Wang, Y., Dai, S., Zhao, P. & Liu, Q. Heart sound signals can be used for emotion recognition. *Scientific Reports* **9**, 6486 (2019).
44. Mao, Q., Li, S. & Liu, W. Development of a sweeping Helmholtz resonator for noise control. *Applied Acoustics* **141**, 348–354 (2018).
45. Wu, D., Zhang, N., Mak, C. M. & Cai, C. Hybrid noise control using multiple Helmholtz resonator arrays. *Applied Acoustics* **143**, 31–37 (2019).
46. Cai, C., Mak, C. M. & Wang, X. Noise attenuation performance improvement by adding Helmholtz resonators on the periodic ducted Helmholtz resonator system. *Applied Acoustics* **122**, 8–15 (2017).
47. Mahesh, K. & Mini, R. Theoretical investigation on the acoustic performance of Helmholtz resonator integrated microperforated panel absorber. *Applied Acoustics* **178**, 108012 (2021).
48. Wang, X., Xu, J., Ding, J., Zhao, C. & Huang, Z. A compact and low-frequency acoustic energy harvester using layered acoustic metamaterials. *Smart Materials and Structures* **28**, 025035 (2019).
49. Nudehi, S. S., Duncan, G. S. & Farooq, U. Modeling and experimental investigation of a Helmholtz resonator with a flexible plate. *Journal of Vibration and Acoustics* **135**, 041102 (2013).
50. Liu, G.-S., Peng, Y.-Y., Liu, M.-H., Zou, X.-Y. & Cheng, J.-C. Broadband acoustic energy harvesting metasurface with coupled Helmholtz resonators. Applied Physics Letters 113 (2018).
51. Zhao, X., Cai, L., Yu, D., Lu, Z. & Wen, J. A low frequency acoustic insulator by using the acoustic metasurface to a Helmholtz resonator. AIP Advances 7 (2017).
52. Almeida, G.dN., Vergara, E. F., Barbosa, L. R., Lenzi, A. & Birch, R. S. A low-frequency sound absorber based on micro-slit and coiled cavity. *Journal of the Brazilian Society of Mechanical Sciences and Engineering* **43**, 1–9 (2021).
53. Wang, Y. et al. A renewable low-frequency acoustic energy harvesting noise barrier for high-speed railways using a Helmholtz resonator and a PVDF film. *Applied Energy* **230**, 52–61 (2018).
54. Alster, M. Improved calculation of resonant frequencies of Helmholtz resonators. *Journal of Sound and Vibration* **24**, 63–85 (1972).
55. Liu, Y. et al. Sound regulation of coupled Helmholtz and Fabry-Pérot resonances in labyrinth cavity structures. *Ultrasonics* **95**, 45–51 (2019).
56. Boccaccio, M., Bucciarelli, F., Fierro, G. P. M. & Meo, M. Microperforated panel and deep subwavelength archimedean-inspired spiral cavities for multi-tonal and broadband sound absorption. *Applied Acoustics* **176**, 107901 (2021).
57. Cai, C., Mak, C.-M. & Shi, X. An extended neck versus a spiral neck of the Helmholtz resonator. *Applied Acoustics* **115**, 74–80 (2017).
58. Guo, J., Zhang, X., Fang, Y. & Qu, R. An extremely-thin acoustic metasurface for low-frequency sound attenuation with a tunable absorption bandwidth. *International Journal of Mechanical Sciences* **213**, 106872 (2022).
59. Chen, Z. Investigations of Helmholtz resonators with curved tapered embedded neck extension. *arXiv preprint arXiv:2309.09852* (2023).
60. Association for the Advancement of Medical Instrumentation. ANSI/AAMI EC13:2002 (R2007) (2002).
61. Emrich, J., Koka, T., Wirth, S. & Muma, M. Accelerated sample-accurate r-peak detectors based on visibility graphs. In *2023 31st European Signal Processing Conference (EUSIPCO)*, 1090–1094 (IEEE, 2023).

62. Koka, T. & Muma, M. Fast and sample accurate r-peak detection for noisy ecg using visibility graphs. In *2022 44th Annual International Conference of the IEEE Engineering in Medicine & Biology Society (EMBC)*, 121–126 (IEEE, 2022).
63. Makowski, D. et al. NeuroKit2: A python toolbox for neurophysiological signal processing. *Behavior Research Methods* **53**, 1689–1696 https://doi.org/10.3758/s13428-020-01516-y (2021).
64. Steinmetz, C. J. & Reiss, J. D. auraloss: Audio focused loss functions in PyTorch. In *Digital music research network one-day workshop (DMRN+ 15)* (2020).
65. Schmalenberg, P. et al. AcousticECG: Non-Invasive Cardiac Sensing via Acoustic Helmholtz Resonator Cavity https://doi.org/10.6084/m9.figshare.31855450.v2 (2026).
66. Schmalenberg, P. et al. Non-invasive cardiac sensing via an acoustic helmholtz resonator cavity with electrocardiogram waveform reconstruction https://doi.org/10.5281/zenodo.21765681 (2026).

Author contributions

P.D.S. conceptualized the approach, designed the resonator, and oversaw the research. P.D.S and E.M.D. performed the numerical simulations for resonator verification and validation. P.D.S., P.S., and F.M.Q.S. oversaw fabrication and post-processing of the hardware resonators. P.S. and F.M.Q.S. configured the data collection environment and performed the collection of the dataset. F.M.Q.S. and B.P conceptualized the data-driven waveform reconstruction approach and proof-of-concept. H.H.S, K.A., and F.M.Q.S. contributed the ConvTASNet implementation, training, and customization for our approach. H.H.S contributed model interpretability, ECG morphology evaluation, and final training and validation of the neural network estimator. E.M.D., H.H.S, P.D.S., K.A., F.M.Q.S., and P.S. contributed substantially to the writing of the manuscript. T.L. advised on the conceptualization of the resonator plus acoustics physics and assisted with editing of the manuscript.

Funding

P.D.S., H.H.S., P.S., F.M.Q.S., T.L., and E.M.D. discloses support for the research in this work from MIRISE Technologies. K.A. and B.P. declare no relevant funding.

Competing interests

P.D.S. and F.M.Q.S. have a United States patent 12,543,964 titled ‘Vehicle heart rate detection device, resonators, and methods of detecting a heart rate.’ P.D.S., K.A., F.M.Q.S., and B.P. have a United States patent pending 20250107770 titled ’Systems and methods for noncontact monitor of cardiac activities.’ All other authors declare no competing interest.

Additional information

Supplementary information The online version contains supplementary material available at https://doi.org/10.1038/s44172-026-00792-4.

Correspondence and requests for materials should be addressed to Paul D. Schmalenberg.

Peer review information *Communications Engineering* thanks all reviewer(s) for their contribution to the peer review of this work. Primary Handling Editors: Rosamund Daw.

Reprints and permissions information is available at http://www.nature.com/reprints

Publisher’s note Springer Nature remains neutral with regard to jurisdictional claims in published maps and institutional affiliations.

Open Access This article is licensed under a Creative Commons Attribution-NonCommercial-NoDerivatives 4.0 International License, which permits any non-commercial use, sharing, distribution and reproduction in any medium or format, as long as you give appropriate credit to the original author(s) and the source, provide a link to the Creative Commons licence, and indicate if you modified the licensed material. You do not have permission under this licence to share adapted material derived from this article or parts of it. The images or other third party material in this article are included in the article's Creative Commons licence, unless indicated otherwise in a credit line to the material. If material is not included in the article's Creative Commons licence and your intended use is not permitted by statutory regulation or exceeds the permitted use, you will need to obtain permission directly from the copyright holder. To view a copy of this licence, visit http://creativecommons.org/licenses/by-nc-nd/4.0/.

© The Author(s) 2026

This Article in Press is shared early to give you faster access to new research. It is citable and carries a permanent DOI. The final edited version will replace it automatically.